Board-level drop reliability and fracture behavior of low-temperature soldering Sn–Ag–Cu/Sn–Bi–X hybrid BGA solder joints for consumer electronics

J. Ren[1] and M. L. Huang[1,*]

[1] *Electronic Packaging Materials Laboratory, School of Materials Science and Engineering, Dalian University of Technology, Dalian 116024, China*

ABSTRACT

Low-temperature soldering technology (185–195 °C) is applied for assembling consumer electronics with various Bi contents, and board-level drop reliability of hybrid Sn–Ag–Cu/Sn–Bi–X ball grid array (BGA) solder joints interconnected chip components and PCB boards was evaluated. A hybrid solder joint structure of a partial melting Sn–Ag–Cu BGA solder ball wrapped by a continuous Bi-containing region was fabricated, and the effects of low Bi content and minor additives of Sn–Bi–X solders on microstructure and board-level drop reliabilities were revealed. The thicker interfacial $Cu_6Sn_5/(Cu,Ni)_6Sn_5$ intermetallic compounds (IMCs) accompanied with larger Bi-rich phases formed at the solder/Cu interface with decreasing Bi content of Sn–Bi–X solder. Drop impact-induced cracks initiated and propagated within the larger Bi-rich phases in a wear-out failure mode, compared with cracks initiated and propagated along the solder/IMC interface in an early failure mode if fine Bi-rich phases segregated at the solder/IMC interface. The Sn–49Bi–1Ag solder was the optimum low-temperature solder for assembling Sn–Ag–Cu/Sn–Bi–X hybrid solder joints, which failed in a wear-out failure mode with the highest drop characteristic lifetime of 420 drops, significantly higher than those failed in an early failure mode.

1 Introduction

Nowadays consumer electronic devices are popular and develop rapidly with the demands of multifunction, miniaturization and green manufacturing. Up to date, the consumer electronic devices are manufactured with thinner printed circuit boards (PCBs), lower Z-height chips and components, and

the ball grid array (BGA) solder balls of 100 μm or less in diameter [1]. Since a typical reflow temperature for Sn–Ag–Cu solder ball is as high as 240–260 °C, the warpage induced by the mismatch between the chips and the substrates due to the different coefficients of thermal expansion (CTE) is becoming an issue. In addition, lower energy consumption and lower cost are also demanded. As a result, low-

---

Address correspondence to E-mail: huang@dlut.edu.cn

temperature soldering technology at 170–200 ℃ is of interest [2].

So far the Sn–Ag–Cu is the dominant solder alloy to make prefabricated BGA solder balls on chips of electronic components [3], which are not easy to be substituted by the low-temperature solders, such as Sn–Bi-based solder balls. Therefore, a novel low-temperature soldering process is applied in assembling hybrid solder joints for consumer electronic devices [4, 5], i.e., the prefabricated Sn–Ag–Cu solder balls on chips of components are hybrid soldered with low-temperature Sn–Bi-based solder pastes, which are stencil printed on substrates such as PCBs. During the assembling process, the molten low-temperature Sn–Bi-based solders wet the Sn–Ag–Cu BGA solder balls to form the hybrid solder joints. The low-temperature soldering of hybrid solder joints can effectively relieve the warpage of the BGA packages of consumer electronic devices.

As for the low-temperature solder alloys, Sn–Bi eutectic solder is one of the highly promising candidates, due to its low melting point, good wettability and low cost [6, 7]. However, there are obvious drawbacks for Sn–Bi eutectic solder, e.g., the high content of Bi in the solder increases the brittleness [8], and Bi atoms tend to segregate and also induce voids at the Cu_3Sn/Cu interface during aging, where cracks initiate and propagate [9, 10]. Therefore, the research on improving the mechanical properties such as drop performance and reducing the brittleness of Sn–Bi-based solder alloys attracts attention.

It is reported that the low content of Bi improves the mechanical properties of the Sn–Bi-based solders. When the Bi content decreased from 58 to 40%, the elongation of solder alloys increased [11]. However, the low content of Bi in Sn–Bi-based solder joints has a limited effect on the improvement of drop property, which is one of the critical properties related to the reliability of consumer electronic devices [12]. Furthermore, the minor additives also influence the microstructure and mechanical properties of the Sn–Bi-based solders joints. Fu [13] reported that a small addition of Ag in the Sn–Bi solder restrained the Bi segregation at the Cu_3Sn/Cu interface, which lowered the embrittlement of solder joints. Other references [14–16] reported that the addition of 3 wt% Sb into the Sn–Ag–Cu alloys increased the ultimate tensile strength (UTS) and creep resistance, which was attributable to the solution strengthening of dissolved Sb atoms in β-Sn, Ag_3Sn and Cu_6Sn_5

phases. The effects of low Bi content and minor additives on the microstructure and board-level drop reliabilities of low-temperature soldering hybrid BGA solder joints are of interest.

In the present work, four types of low-temperature Sn–Bi–X solders with lower Bi content than that of Sn–Bi eutectic and minor additives were used to assemble the chips of components with prefabricated Sn–3.0Ag–0.5Cu BGA solder balls and the PCB substrates. The microstructure and the board-level drop reliability of these low-temperature Sn–Ag–Cu/Sn–Bi–X hybrid solder joints were investigated.

2 Experimental

The test vehicle involves a silicon chip of 27 mm × 27 mm × 2.13 mm in size, which interconnected to a PCB of 103 mm × 52 mm × 1.60 mm in size. The UBM on the chip is Ni of 15 μm thick, and the pad finish on the PCB is an organic solderability preservative (OSP) of 60 μm thick. 733 Sn–3.0Ag–0.5Cu solder balls of 500 μm in diameter were prefabricated on the chip. Four types of low-temperature Sn–Bi–X solder pastes of 180 μm in thickness were stencil printed on the PCB, as listed in Table 1. The hybrid solder joints were soldered under various reflow profiles (185–195 ℃) to achieve a Bi mixing percentage of 40–50%—the area of Bi distribution occupied the area of the whole hybrid solder joint [17].

Board-level drop impact test system (JEDEC, Salon Teknopaja Oy, Finland) was used to assess the drop reliability of test vehicles, according to the Joint Electron Devices Engineering Council (JEDEC) standards of JESD22-B111 and JESD22-B104C. Figure 1 shows the schematic configuration of the drop impact test system. The PCB boards of test vehicles were fixed at the four corners of the drop table with the mounted BGA components facing downward. The equivalent drop height was 180 mm, the acceleration peak was 270 g, and the pulse duration was 1.55 ms. For each type of low-temperature Sn–Bi–X solder paste, 32 specimens were tested to obtain a high confidence coefficient of 95%. A real-time resistance measurement system was used to monitor the drop failures of the test vehicles. The failure criterion was defined as the case in which the overall electrical resistance of the solder joints of a component board exceeds 999 Ω during two consecutive drops.

Table 1 Information of Sn–Bi–X solders

Alloy type	Compositions (wt%)	Melting temperature (°C)	Flux type
Sn–40Bi–2Sb	Sn–40Bi–2Sb	143–144	ROL0
Sn–49Bi–1Ag	Sn–49Bi–(0.8–1.2)Ag + 1Additives	138–151	ROL0
Sn–57Bi–1Ag	Sn–57Bi–1Ag	138	ROL0
Sn–58Bi–1Sb–1Ni	Sn–58Bi–1Sb–1Ni	140–145	ROL0
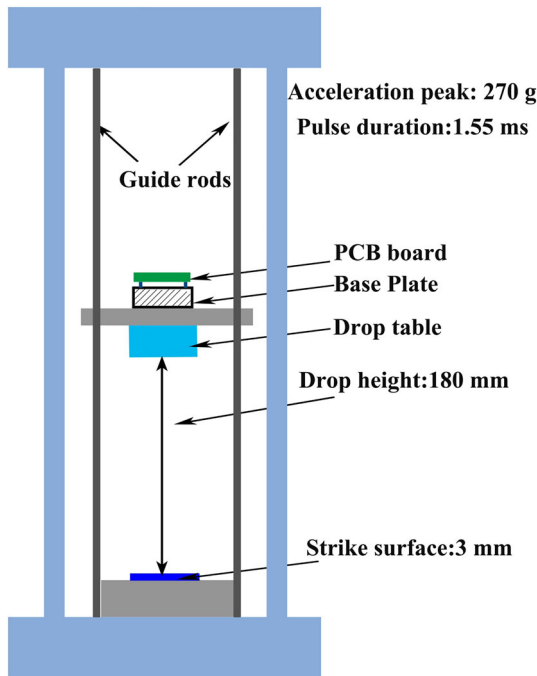
Fig. 1 Schematic configuration of drop impact test system

Fig. 2 Cross-sectional microstructure of low-temperature Sn–Ag–Cu/Sn–Bi–X hybrid solder joint in as-soldered state

Test vehicle specimens were prepared for cross-sectional analyses before and after the failure. A Zeiss Supra 55 scanning electron microscope (SEM) and a JXA-8530 F Plus Hyper Probe field-emission electron probe micro-analyzer (EPMA) were employed to investigate the microstructure of hybrid solder joints.

3 Results

3.1 Microstructure of Sn–Ag–Cu/Sn–Bi–X hybrid solder joints

Figure 2 shows the cross-sectional microstructure of a low-temperature soldering Sn–Ag–Cu/Sn–Bi–X hybrid solder joint in the as-soldered state. The low-temperature soldering process caused partial melting
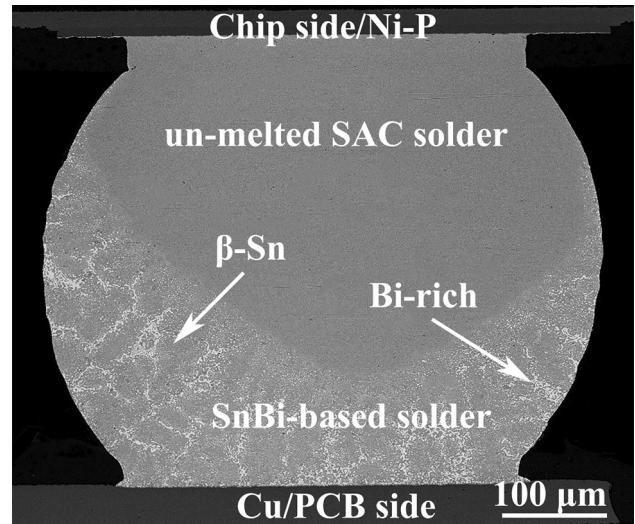
of Sn–Ag–Cu solder ball, and consequently an inhomogeneous microstructure of the hybrid solder joint was observed, of which the un-melted Sn–Ag–Cu solder ball was partially wrapped by the low-temperature Sn–Bi–X solder.

Figure 3 shows the enlarged SEM images of interfacial microstructure at the solder/PCB interfaces of hybrid solder joints. Scalloped Cu_6Sn_5 intermetallic compound (IMC) grains formed at the Sn–Bi–X/Cu interfaces of Sn–40Bi–2Sb, Sn–49Bi–1Ag, Sn–57Bi-1Ag hybrid solder joints, and $(Cu_{0.9}Ni_{0.1})_6Sn_5$ grains formed at the interface of Sn–58Bi–1Sb–1Ni hybrid solder joint. However, the thickness of interfacial IMC layer varied with the Bi content of solder joints, which was in an order of Sn–40Bi–2Sb (1.93 μm) > Sn–49Bi–1Ag (1.81 μm) > Sn–57Bi-1Ag (0.81 μm) > Sn–58Bi–1Sb–1Ni (0.58 μm), i.e., the higher Bi content resulted in the thinner interfacial IMC.

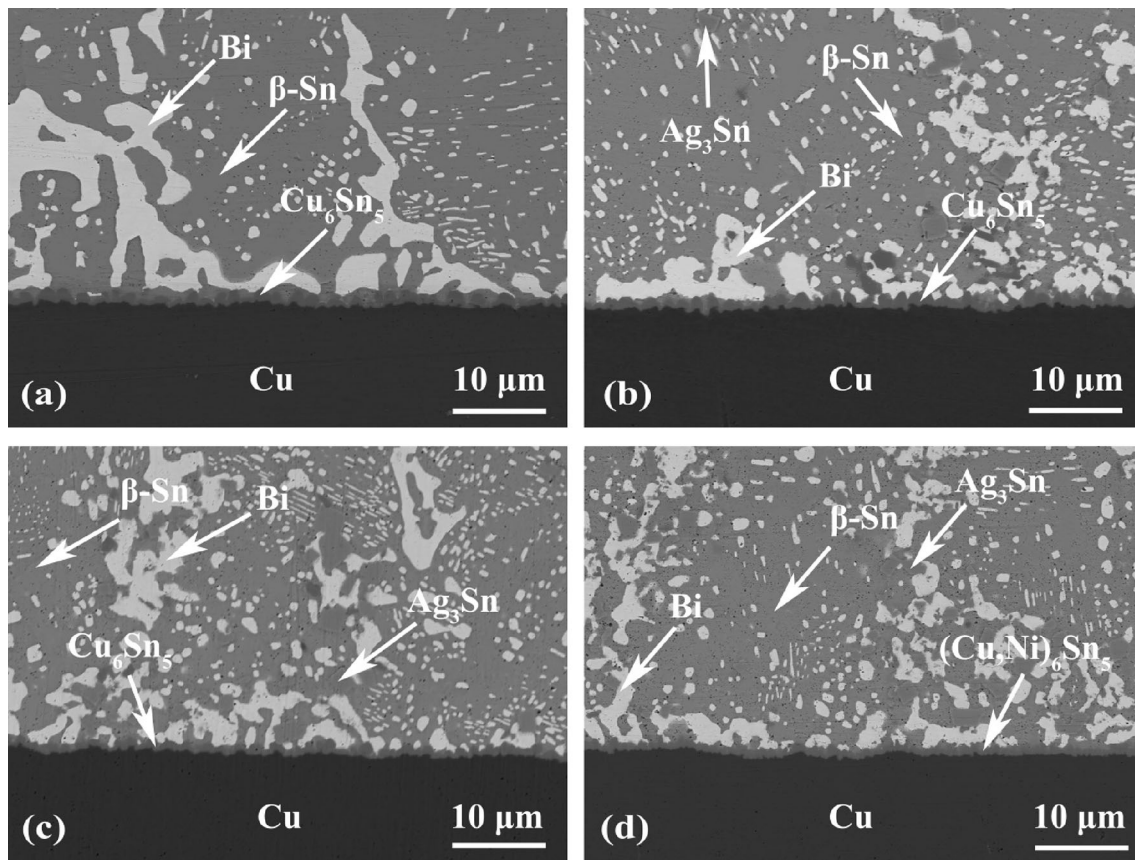Moreover, abundant discontinuously Bi-rich phases randomly segregated in front of the solder/

Fig. 3 Enlarged SEM images of interfacial microstructure (PCB side) with different Sn–Bi–X solders: **a** Sn–40Bi–2Sb, **b** Sn–49Bi–1Ag, **c** Sn–57Bi–1Ag and **d** Sn–58Bi–1Sb–1Ni

Cu_6Sn_5 interface, since Bi atoms were not involved in the interfacial reaction during the low-temperature soldering. As shown in Fig. 3, the size of Bi-rich phase also follows a descending order of Sn–40Bi–2Sb (4.94 μm) > Sn–49Bi–1Ag (3.85 μm) > Sn–57Bi–1Ag (2.97 μm) > Sn–58Bi–1Sb–1Ni (2.45 μm). It seemed that the thicker the interfacial Cu_6Sn_5 IMC formed, the more the Bi-rich phases segregated in front of the solder/Cu_6Sn_5 interface.

Figure 4 shows the top-view SEM images of interfacial Cu_6Sn_5 grains at the Sn–Bi–X/Cu interface of hybrid solder joints in the as-soldered state. The average diameters of Cu_6Sn_5 grains were 0.65, 0.61, 0.54 and 0.20 μm for Sn–40Bi–2Sb, Sn–49Bi–1Ag, Sn–57Bi–1Ag and Sn–58Bi–1Sb–1Ni hybrid solder joints, respectively, which were in good agreement with the IMC thicknesses, as shown in Fig. 3.

3.2 Drop impact and fracture behavior of Sn–Ag–Cu/Sn–Bi–X hybrid solder joints

Figure 5a shows the Weibull plots of cumulative failure probability of the test vehicle hybrid solder joints. The Weibull probability distribution function was expressed by [18]:

$$F(t) = 1 - \exp\left[-\left(\frac{t}{\lambda}\right)^{\kappa}\right], \tag{1}$$

where $F(t)$ is the cumulative failure probability, t is the number of drops to failure, κ is the shape parameter, and λ is the scale parameter. κ and λ values reflect the dispersion of lifetime and characteristic lifetime of the hybrid solder joints, respectively.
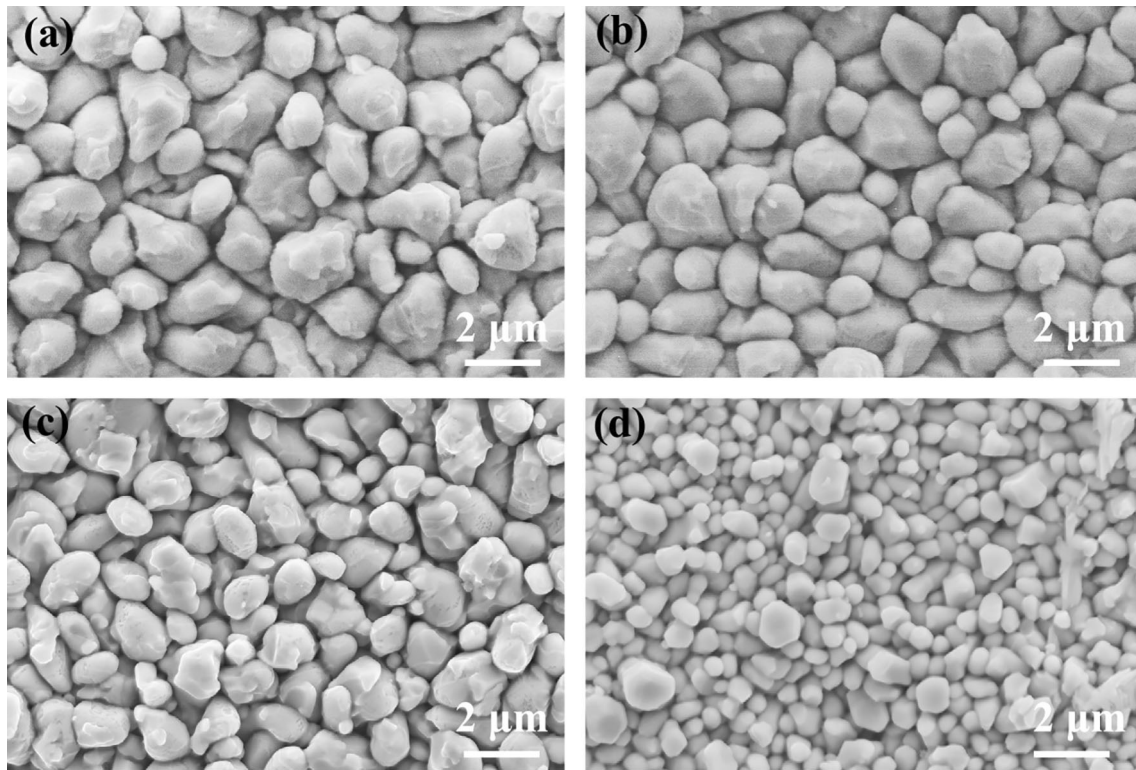
Fig. 4 Top-view images of interfacial Cu$_6$Sn$_5$ grains (PCB side) with different Sn–Bi–X solders: **a** Sn–40Bi–2Sb, **b** Sn–49Bi–1Ag, **c** Sn–57Bi–1Ag and **d** Sn–58Bi–1Sb–1Ni

The characteristic lifetimes λ were 247, 482, 320 and 202 drops for Sn–40Bi–2Sb, Sn–49Bi–1Ag, Sn–57Bi–1Ag and Sn–58Bi–1Sb–1Ni hybrid solder joints, respectively. Further considering the 10% of cumulative failure, the lifetimes were 15, 84, 9 and 7 drops for Sn–40Bi–2Sb, Sn–49Bi–1Ag, Sn–57Bi–1Ag and Sn–58Bi–1Sb–1Ni hybrid solder joints, respectively. It was shown that the Sn–49Bi–1Ag hybrid solder joints exhibited a superior drop resistance than the Sn–40Bi–2Sb, Sn–58Bi–1Sb–1Ni and Sn–57Bi–1Ag hybrid solder joints.

Moreover, the dispersion of lifetime κ for Sn–49Bi–1Ag hybrid solder joints was 1.29, which was higher than those of 0.80, 0.64 and 0.67 for Sn–40Bi–2Sb, Sn–57Bi–1Ag and Sn–58Bi–1Sb–1Ni hybrid solder joints, respectively. Figure 5b shows the Weibull probability failure density distribution plots of the test vehicle hybrid solder joints. The density distribution function was expressed by:

$$f(t) = \kappa\lambda^{-\kappa}t^{\kappa-1}\exp\left[-\left(\frac{t}{\lambda}\right)^{\kappa}\right]. \tag{2}$$

The shape of density distribution for Sn–49Bi–1Ag hybrid solder joints is convex, showing a wear-out failure mode, which means the hybrid solder joints preferred to fail at the later stage of the drop tests. However, the shapes of density distributions for Sn–40Bi–2Sb, Sn–57Bi–1Ag and Sn–58Bi–1Sb–1Ni hybrid solder joints are concave, showing early failure modes, which mean the hybrid solder joints preferred to fail at the early stage of the drop tests. Thus, the Sn–49Bi–1Ag hybrid solder joints showed a significant enhancement in the drop impact reliability, compared to the Sn–40Bi–2Sb, Sn–57Bi–1Ag and Sn–58Bi–1Sb–1Ni hybrid solder joints.

Figure 6 shows the crack locations in hybrid solder joints that failed at the characteristic lifetime. As shown in Fig. 6b, the Sn–49Bi–1Ag hybrid solder bumps completely separated from the Cu substrate along the interfacial IMC, while in the Sn–40Bi–2Sb,
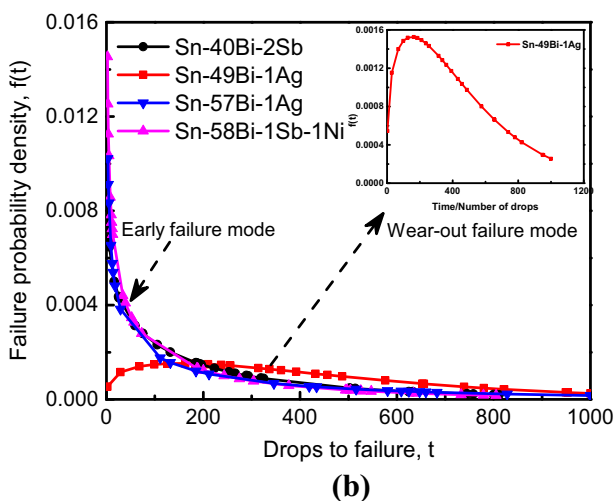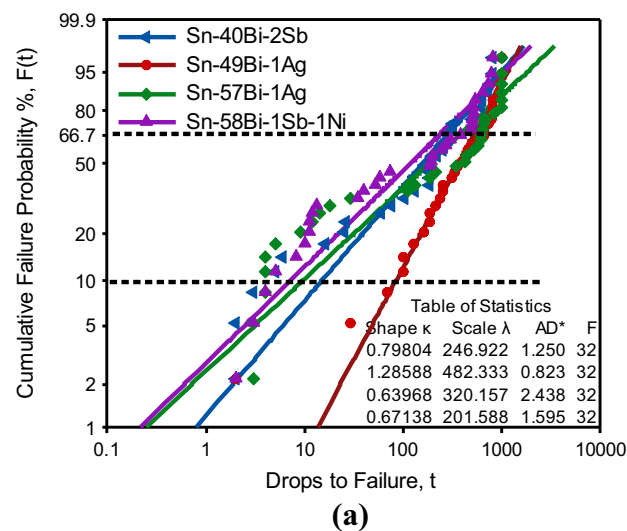
Fig. 5 Weibull plots of cumulative failure probability (**a**) and failure probability density distributions (**b**) of hybrid solder joints with different Sn–Bi–X solders

Sn–57Bi–1Ag and Sn–58Bi–1Sb–1Ni hybrid solder joints, small cracks located at the solder/Cu interfaces, and the solder joints still kept integrity, as shown in Fig. 6a, c, d. Therefore, the Sn–49Bi–1Ag hybrid solder joints failed in the wear-out failure modes has a longer critical crack length, compared to the other three hybrid solder joints failed in the early failure modes.

Figure 7 shows the EPMA mapping analysis of fracture surfaces on the PCB side, corresponding to Fig. 6a–d. As shown in Fig. 7a and b, in the Sn–40Bi–2Sb and Sn–49Bi–1Ag hybrid solder joints, a high

content of Bi remained and occupied the most region of fracture surface, whereas Sn and Cu partially preserved in the other sections, confirming that fracture mostly occurred within the Bi-rich phases. However, in the Sn–57Bi–1Ag and Sn–58Bi–1Sb–1Ni hybrid solder joints, high contents of Sn and Cu were observed across the entire fracture surfaces, showing that the drop fracture occurred across the IMC layer, as shown in Fig. 7c and d. Bi was also detected in the fracture surfaces, but the sizes of Bi phases of Sn–57Bi–1Ag and Sn–58Bi–1Sb-1Ni hybrid solder joints were much smaller than those of Sn–40Bi–2Sb and Sn–49Bi–1Ag ones.

4 Discussion

4.1 Effect of Bi content on microstructure of hybrid solder joints

Figure 8 shows the average Bi contents in the Bi mixing regions of hybrid solder joints. In the as-soldered state, the Bi content varied from 17.4 to 23.7 wt%, and followed an order of Sn–40Bi–2Sb < Sn–49Bi–1Ag < Sn–57Bi–1Ag < Sn–58Bi–1Sb–1Ni. According to the Sn–Bi phase diagram [19], the alloy with a lower Bi content has a higher liquidus temperature. As a result, to obtain a similar Bi mixing percentage in hybrid solder joints, a higher soldering temperature is required for the hybrid solder joints with a lower Bi content. Moreover, a lower Bi content also resulted in an increase in the kinetics of interfacial reaction, since Bi atoms were not involved in the interfacial reaction. Thus, the lower the Bi content of solder joints was, the thicker the IMC layer formed.

Moreover, based on the concentration gradient control (CGC) interfacial reaction model [20, 21], the size of Bi phases was mainly controlled by the Bi influx, i.e., the flux of Bi atoms flowing toward the front of solder/IMC interface ($J_{inter/Bi}$). In the as-soldered state, the Bi influx was mainly supplied by the segregation flux ($J_{pre/Bi}$), while it was consumed by the up-diffusion flux ($J_{up/Bi}$) of Bi atoms due to the low concentration of un-melted SAC region. Therefore, the influx of Bi atoms could be expressed by:
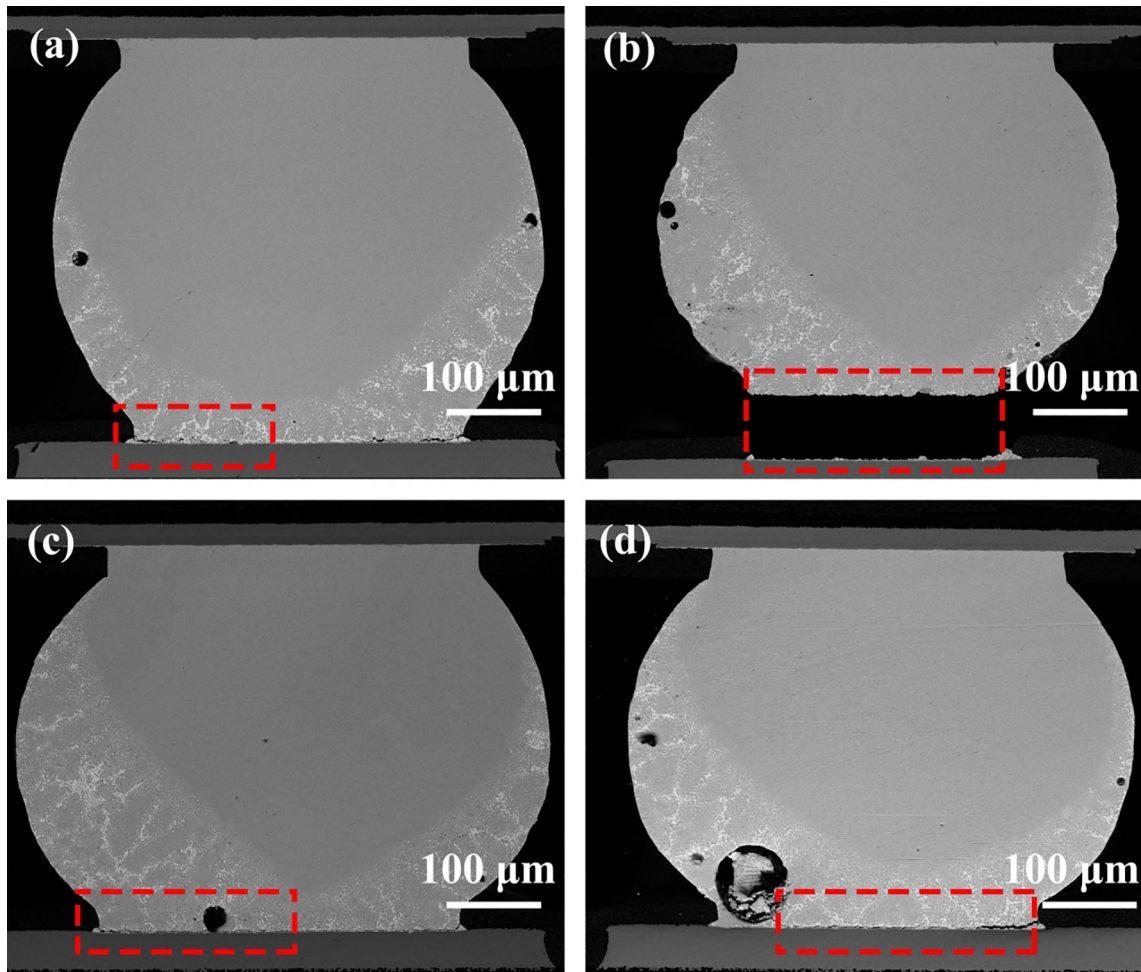
Fig. 6 Crack locations in hybrid solder joints after drop impact failure at characteristic life times of **a** Sn–40Bi–2Sb, **b** Sn–49Bi–1Ag, **c** Sn–57Bi–1Ag and **d** Sn–58Bi–1Sb–1Ni

$$J_{\text{inter/Bi}} = J_{\text{seg/Bi}} - J_{\text{up/Bi}} \propto \text{Bi}_{\text{size}} \tag{3}$$

Since Bi atoms were not involved in the interfacial reaction, a thicker IMC formation resulted in a higher Bi segregation at the front of solder/IMC interface. As a result, $J_{\text{seg/Bi}}$ of hybrid solder joints with lower Bi content is higher than that of hybrid solder joints with the higher Bi content, that is $J_{\text{seg/Bi}}^{\text{low}} > J_{\text{seg/Bi}}^{\text{high}}$.

After reflow, although the difference in Bi content between Sn–49Bi–1Ag and Sn–57Bi–1Ag solders decreased from 8 to 2 wt% (Fig. 8), the up-diffusion of Bi atoms in hybrid solder joints with the higher Bi content was still higher than that with the lower Bi content, which means $J_{\text{up/Bi}}^{\text{low}} < J_{\text{up/Bi}}^{\text{high}}$.

Based on Eq. 3, it was concluded that $J_{\text{inter/Bi}}^{\text{low}} > J_{\text{inter/Bi}}^{\text{high}}$. Therefore, the hybrid solder joints with a lower Bi content precipitated large Bi phases.

4.2 Effects of minor additives on microstructure of hybrid solder joints

As shown in Fig. 4, the grains of interfacial Cu_6Sn_5 with minor additives of Sb and Ni were remarkably finer than those with Ag addition. Figure 9 shows the elemental mapping of Cu, Sn, Ag, Sb, Ni and Bi for the four types of Sn–Bi–X solders. Ag addition induced the formation of Ag_3Sn in the β-Sn matrix
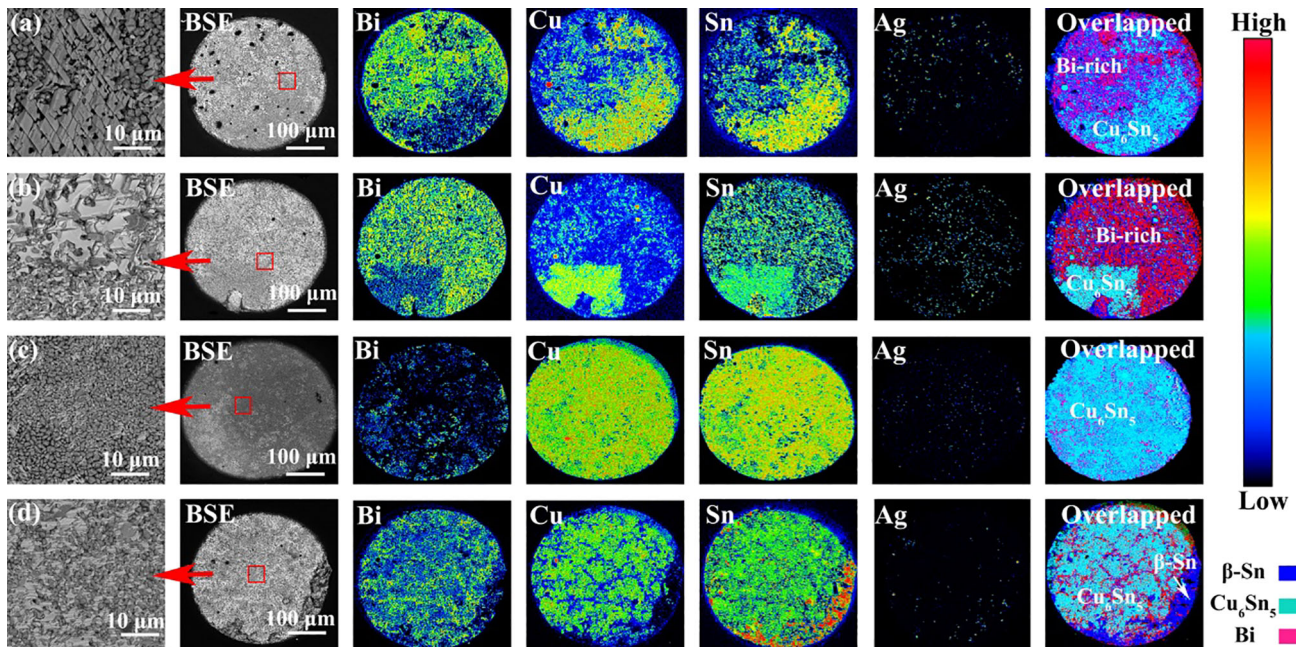
Fig. 7 EPMA mapping analysis results of drop failure fracture surface (PCB side) with different Sn–Bi–X solders: **a** Sn–40Bi–2Sb, **b** Sn–49Bi–1Ag, **c** Sn–57Bi–1Ag and **d** Sn–58Bi–1Sb–1Ni
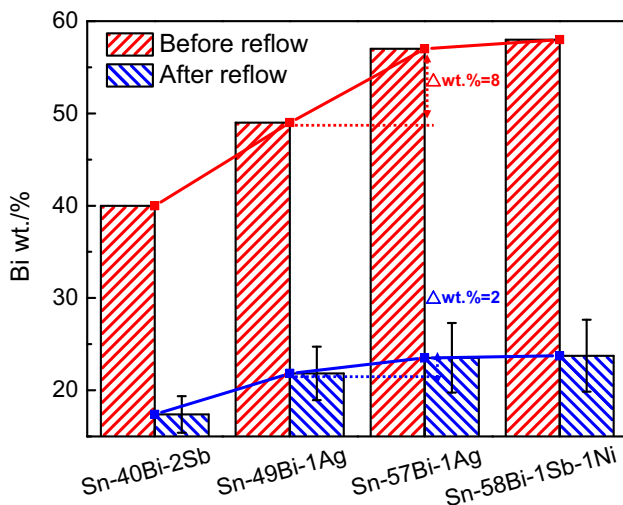

Fig. 8 Average Bi contents in Bi mixing regions of hybrid solder joints

(Fig. 9b and c), while Sb and Ni formed a solid solution in β-Sn (Fig. 9a and d).

The addition of Ag into the Sn–Bi-based solder was reported to decrease the brittleness and improve the

mechanical properties [22, 23]. The Ag$_3$Sn particles formed in the β-Sn solder matrix can effectively hinder the movement of interfacial dislocations due to the pining effect. Consequently, the Sn–49Bi–1Ag and Sn–57Bi–1Ag hybrid solder joints with the Ag addition exhibited superior drop reliability. In comparison, Sb and Ni additives significantly improved the UTS but depressed the elongation of solder joints, due to the stronger solid-solution hardening and particle hardening effects [15, 16]. As a result, the worse drop reliability was obtained for the Sn–40Bi–2Sb and Sn–58Bi–1Sb-1Ni hybrid solder joints.

Moreover, it was reported that the addition of 1.0 wt% Sb into Sn–3.0Ag–0.7Cu solder led to the formation of Ag$_3$(Sn,Sb) IMC layers, and thus decreased the grain size of Cu–Sn IMCs [24]. That is why the thickness of IMCs in Sn–58Bi–1Sb–1Ni hybrid solder joints was approximately half of that in Sn–57Bi–1Ag ones, as shown in Fig. 3. Consequently, smaller Bi-rich phases formed in front of solder/Cu interface for hybrid solder joints with Sb and Ni additions compared to that with Ag addition.
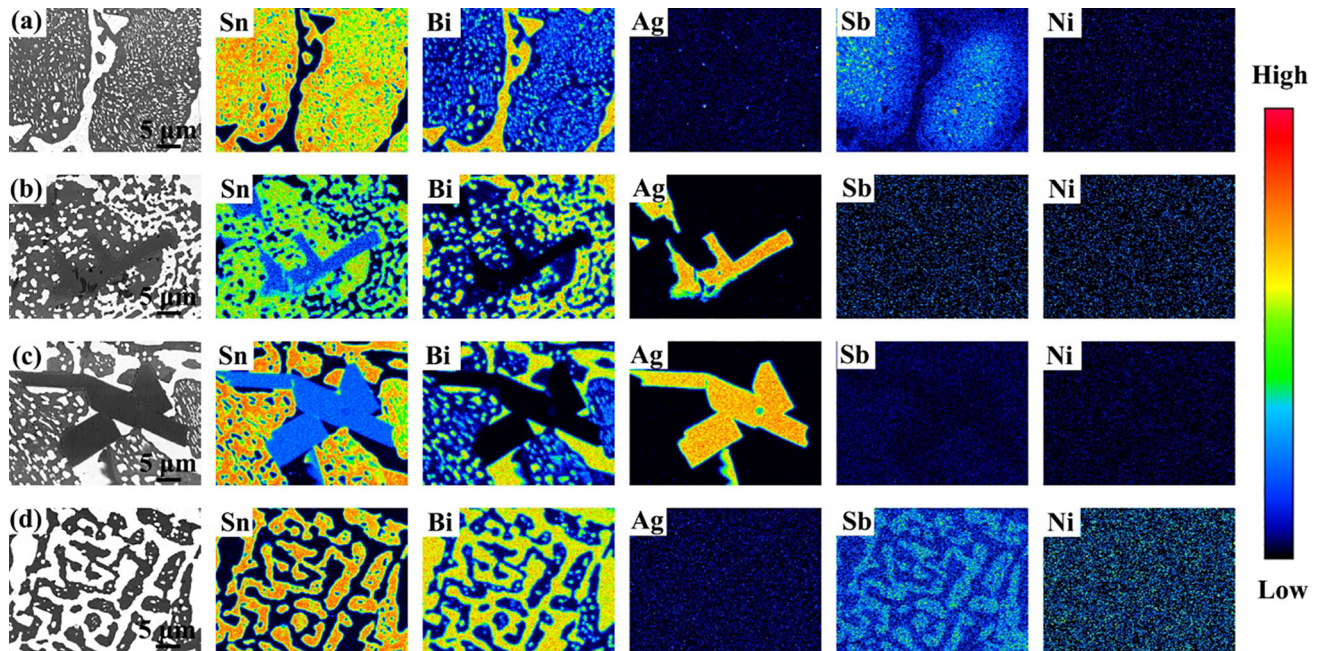
Fig. 9 EPMA map scanning of different bulk Sn–Bi–X solder alloys: **a** Sn–40Bi–2Sb, **b** Sn–49Bi–1Ag, **c** Sn–57Bi–1Ag and **d** Sn–58Bi–1Sb–1Ni

4.3 Distribution of Bi phases in hybrid solder joints

Figure 10 shows the interfacial microstructure at the PCB side of Sn–49Bi–1Ag hybrid solder joints. Cracks were inclined to propagate within the large Bi-rich phases that segregated at the solder/IMC interface, and the secondary cracks were also observed, as shown in Fig. 10c. It was indicated that the cracks were inclined to propagate in the large Bi-rich phases to relax the stress concentration, due to the lower elastic modulus of Bi phase (25 GPa) than those of pure Sn (44 GPa) and $(Cu,Ni)_6Sn_5$ (100–210 GPa) [25–27]. The large Bi-rich phases had higher stress compliance and higher plastic energy dissipation ability during the crack propagation process, which effectively toughened the crack tip and prolonged the lifetime to reach the critical rupture stress.

Moreover, the segregated large Bi-rich phases consist of fine Bi grains with diameters lower than 1 µm, as shown in Fig. 10b. Fine grains further prolonged the crack paths. The appearance of the secondary crack tips during the drop impact tests released and redistributed the stress, absorbed the energy and deferred the main crack propagation. Therefore, the hybrid solder joints with large Bi-rich phases exhibited superior drop properties with a wear-out failure mode.

As to the fine Bi-rich phases segregated in front of the solder/IMC interface, according to the Orowan mechanism [28–31], cracks preferentially propagated at the weaker solder/IMC interface rather than across the Bi particles, as shown in Fig. 11. Therefore, the hybrid solder joints with fine Bi-rich phases were inclined to fail in an early failure mode with poor drop properties.

Figure 12 shows the schematic of hybrid solder joints with two different failure modes. For the wear-out failure mode, large Bi-rich phases segregated in front of the solder/IMC interface, and the drop impact-induced crack occurred at the corner of solder joints and subsequently propagated and derived the secondary cracks within the Bi-rich phases. For the early failure mode, fine Bi-rich phases segregated and
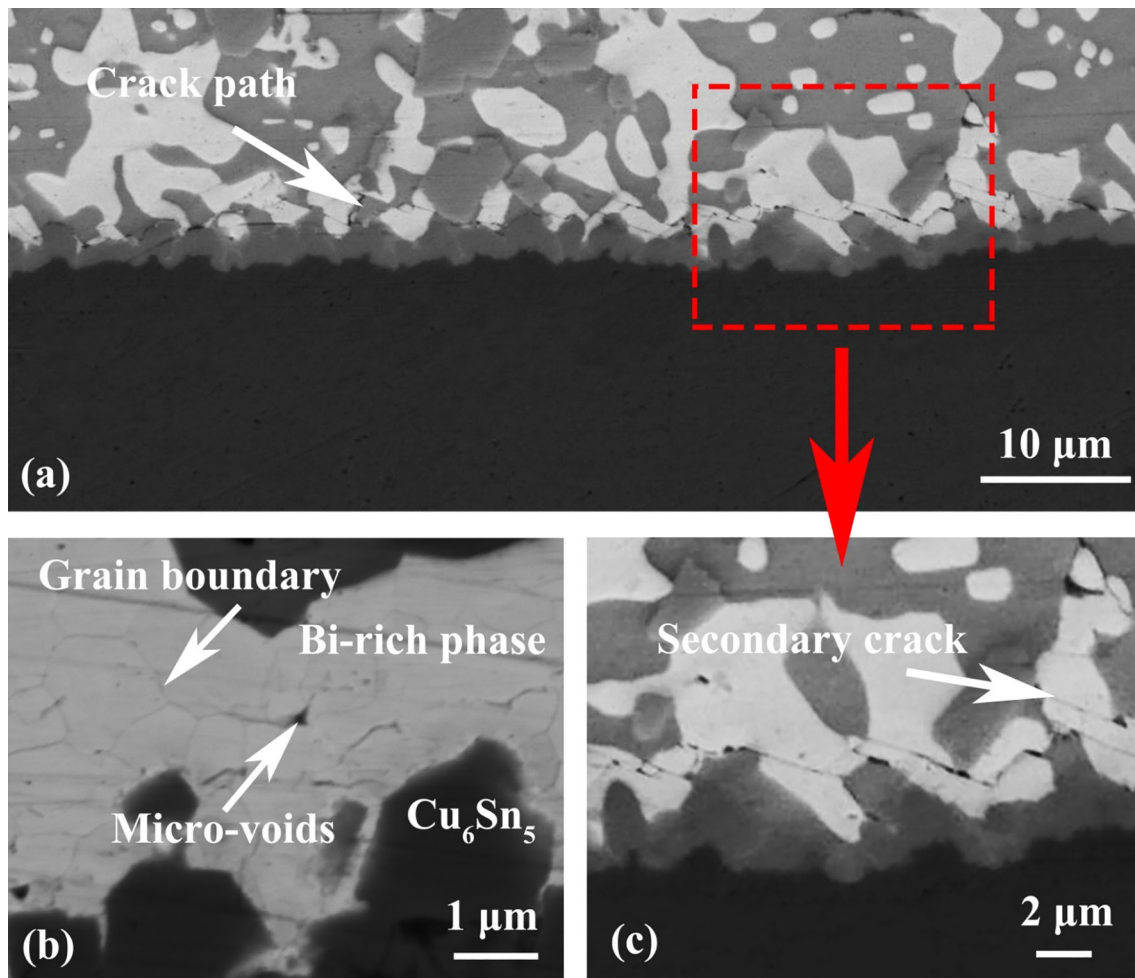
Fig. 10 Cross-sectional drop impact failure fracture morphologies (PCB side) of Sn–49Bi–1Ag hybrid solder joints: **a** crack path, **b** and **c** enlarged images of Bi-rich phase and crack path in (**a**), respectively
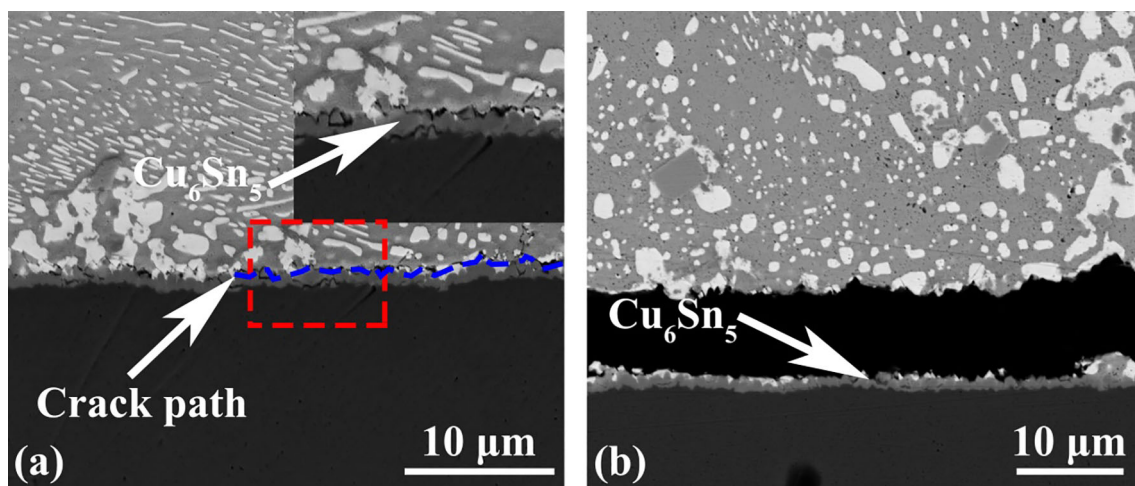

Fig. 11 Cross-sectional drop impact failure fracture morphologies (PCB side) of Sn–58Bi–1Sb-1Ni hybrid solder joints, **a** crack path in integrate solder joint, **b** bumps separated from PCB, respectively
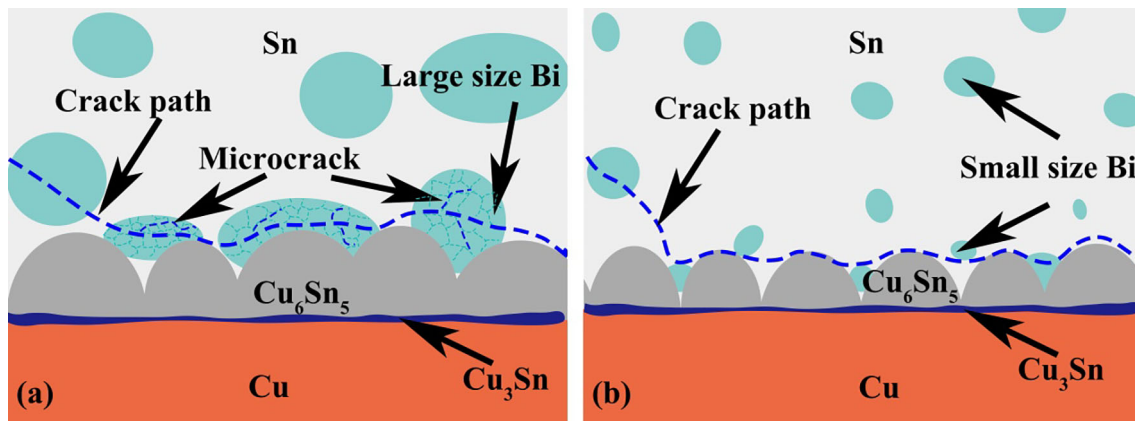
Fig. 12 Schematic of interfacial microstructure at PCB side of hybrid solder joints with two different failure modes: **a** wear-out failure mode and **b** early failure mode

the cracks propagated along the solder/IMC interface.

5 Conclusions

1. With decreasing Bi content in Sn–Bi–X solder, the thicker interfacial Cu_6Sn_5 or $(Cu,Ni)_6Sn_5$ IMC accompanied with larger Bi-rich phases formed at the solder/Cu interface of low-temperature soldering Sn–Ag–Cu/Sn–Bi–X hybrid solder joints, due to the lower Bi concentration gradient and higher reflow temperature.

2. The addition of Ag promoted the formation of Ag_3Sn particles with a pinning effect, while the minor additives of Sb and Ni formed a solid solution in β-Sn matrix and hindered the growth of interfacial $Cu_6Sn_5/(Cu,Ni)_6Sn_5$ grains.

3. If large Bi-rich phases segregated in front of solder/IMC interface of hybrid solder joints, drop impact-induced cracks initiated and propagated within Bi-rich phases and the hybrid solder joints failed in a wear-out failure mode, while if fine Bi-rich phases segregated, drop impact-induced cracks initiated and propagated along the solder/IMC interface and the hybrid solder joints failed in an early failure mode.

4. Combined with microstructure and board-level drop reliability, Sn–49Bi–1Ag solder was the optimum low-temperature solder for assembling Sn–Ag–Cu/Sn–Bi–X hybrid solder joints, which failed in a wear-out failure mode with the highest drop characteristic lifetime of 420 drops, 138.6, 50.6 and 95.9% higher than those of Sn–40Bi–2Sb,

Sn–57Bi–1Ag and Sn–58Bi–1Sb-1Ni hybrid solder joints failed in an early failure mode, respectively.

Data availability

The raw/processed data required to reproduce these findings cannot be shared at this time as the data also form part of an ongoing study.

Declarations

Conflict of interest No conflict of interest exits in the submission of this manuscript, and manuscript is approved by all authors and the responsible authorities at the institute for publication.

References

1. M.L. Huang, J.F. Zhao, Z.J. Zhang, N. Zhao, Role of diffusion anisotropy in β-Sn in microstructural evolution of Sn–3.0Ag–0.5Cu flip chip bumps undergoing electromigration. Acta Mater. **100**, 98–106 (2015). https://doi.org/10.1016/j.actamat.2015.08.037

2. S. Sahasrabudhe, S. Mokler, M. Renavikar, S. Sane, K. Byrd, E. Brigham et al., Low temperature solder—a breakthrough

technology for surface mounted devices, in *2018 IEEE Electronic Components and Technology Conference* (2018), pp. 1455–1464. https://doi.org/10.1109/ECTC.2018.00222

3. W.A. Siswanto, M. Arun, I.V. Krasnopevtseva, A. Surendar, A. Maseleno, A competition between stress triaxiality and joule heating on microstructure evolution and degradation of SnAgCu solder joints. J. Manuf. Processes **54**, 221–227 (2020). https://doi.org/10.1016/j.jmapro.2020.03.016

4. Y.H. Jo, J.W. Lee, S.K. Seo, H.M. Lee, H. Han, D.C. Lee, Demonstration and characterization of Sn–3.0Ag–0.5Cu/Sn–57Bi–1Ag combination solder for 3-D multistack packaging. J. Electron. Mater. **37**, 110–117 (2008). https://doi.org/10.1007/s11664-007-0296-0

5. T.T. Chou, R.W. Song, H. Chen, J.G. Duh, Low thermal budget bonding for 3D-package by collapse-free hybrid solder. Mater. Chem. Phys. **238**, 121887 (2019). https://doi.org/10.1016/j.matchemphys.2019.121887

6. J.H. Wang, L. Wen, J.W. Zhou, M. Chung, Mechanical properties and joint reliability improvement of Sn–Bi alloy, in *2011 IEEE 13th Electronics Packaging Technology Conference* (2011), pp. 492–496. https://doi.org/10.1109/EPTC.2011.6184470

7. K.N. Tu, K. Zeng, Tin-lead (SnPb) solder reaction in flip chip technology. Mater. Sci. Eng. R Rep. **34**, 1–58 (2001). https://doi.org/10.1016/S0927-796X(01)00029-8

8. Y. Goh, A.S.M.A. Haseeb, M.F.M. Sabri, Effects of hydroquinone and gelatin on the electrodeposition of Sn–Bi low temperature Pb-free solder. Electrochim. Acta **90**, 265–273 (2013). https://doi.org/10.1016/j.electacta.2012.12.036

9. P.J. Shang, Z.Q. Liu, D.X. Li, J.K. Shang, Directional growth of Cu₃Sn at the reactive interface between eutectic SnBi solder and (100) single crystal Cu. Scripta Mater. **59**, 317–320 (2008). https://doi.org/10.1016/j.scriptamat.2008.03.031

10. P.L. Liu, J.K. Shang, Interfacial embrittlement by bismuth segregation in copper/tin–bismuth Pb-free solder interconnect. J. Mater. Res. **16**, 1651–1659 (2001). https://doi.org/10.1557/JMR.2001.0229

11. H. Takao, A. Yamada, H. Hasegawa, M. Matsui, Mechanical properties and solder joint reliability of low-melting Sn–Bi–Cu lead free solder alloy. J. Jpn. Inst. Electron. Packag. **5**, 152–158 (2002). https://doi.org/10.5104/jiep.5.152

12. M. Ribas, A. Kumar, D. Kosuri, R.R. Rangaraju, P. Choudhury, S. Telu et al., Low temperature soldering using Sn–Bi alloys, in *Proceedings of SMTA International* (2017), pp. 17–21

13. F.Q. Hu, Q.K. Zhang, J.J. Jiang, Z.L. Song, Influences of Ag addition to Sn–58Bi solder on SnBi/Cu interfacial reaction. Mater. Lett. **214**, 142–145 (2018). https://doi.org/10.1016/j.matlet.2017.11.127

14. M. Celikin, M. Maalekian, M. Pekguleryuz, Effect of Sb Additions on the Creep Behaviour of Bi Containing SAC Alloys. J. Electron. Mater. **48**, 5562–5569 (2019). https://doi.org/10.1007/s11664-019-07410-4

15. Q.B. Tao, L. Benabou, T.A. Nguyen Van, H. Nguyen-Xuan, Isothermal aging and shear creep behavior of a novel lead-free solder joint with small additions of Bi, Sb and Ni. J. Alloy. Compd. **789**, 183–192 (2019). https://doi.org/10.1016/j.jallcom.2019.02.316

16. A.A. El-Daly, A.E. Hammad, A. Fawzy, A. Nasrallh, Microstructure, mechanical properties, and deformation behavior of Sn–1.0Ag–0.5Cu solder after Ni and Sb additions. Mater. Des. **43**, 40–49 (2013). https://doi.org/10.1016/j.matdes.2012.06.058

17. H. Fu, R. Aspandiar, J. Chen, S. Cheng, Q. Chen, R. Coyle et al., INEMI project on process development of BISN-based low temperature solder pastes—Part II: characterization of mixed alloy BGA solder joints, in *2018 Pan Pacific Microelectronics Symposium* (2018), pp. 1–17. https://doi.org/10.23919/PanPacific.2018.8318989

18. W. Weibull, S. Sweden, A statistical distribution function of wide applicability. J. Appl. Mech. **18**, 293–297 (1951). https://doi.org/10.1115/1.4010337

19. P.L. Lin, A.D. Pelton, C.W. Bale, An interactive computer program for calculating ternary phase diagrams. Calphad **4**, 47–60 (1980). https://doi.org/10.1016/0364-5916(80)90019-X

20. M.L. Huang, F. Yang, N. Zhao, Z.J. Zhang, In situ study on dissolution and growth mechanism of interfacial Cu₆Sn₅ in wetting reaction. Mater. Lett. **139**, 42–45 (2015). https://doi.org/10.1016/j.matlet.2014.10.041

21. M.L. Huang, F. Yang, Size effect model on kinetics of interfacial reaction between Sn-xAg-yCu solders and Cu substrate. Sci. Rep. **4**, 1–9 (2014). https://doi.org/10.1038/srep07117

22. W.R. Myung, M.K. Ko, Y. Kim, S.B. Jung, Effects of Ag content on the reliability of LED package component with Sn–Bi–Ag solder. J. Mater. Sci. Mater. Electron. **26**, 8707–8713 (2015). https://doi.org/10.1007/s10854-015-3546-6

23. B.L. Silva, M.G.C. Xavier, A. Garcia, J.E. Spinelli, Cu and Ag additions affecting the solidification microstructure and tensile properties of Sn–Bi lead-free solder alloys. Mater. Sci. Eng. A **705**, 325–334 (2017). https://doi.org/10.1016/j.msea.2017.08.059

24. B.L. Chen, G.Y. Li, Influence of Sb on IMC growth in Sn–Ag–Cu–Sb Pb-free solder joints in reflow process. Thin Solid Films **462–463**, 395–401 (2004). https://doi.org/10.1016/j.tsf.2004.05.063

25. D. Mu, H. Huang, S.D. McDonald, J. Read, K. Nogita, Investigating the mechanical properties, creep and crack pattern of Cu_6Sn_5 and $(Cu,Ni)_6Sn_5$ on diverse crystal planes. Mater. Sci. Eng. A **566**, 126–133 (2013). https://doi.org/10.1016/j.msea.2012.12.057

26. L. Shen, P. Septiwerdani, Z. Chen, Elastic modulus, hardness and creep performance of SnBi alloys using nanoindentation. Mater. Sci. Eng. A **558**, 253–258 (2012). https://doi.org/10.1016/j.msea.2012.07.120

27. L. Xu, J.H.L. Pang, Nano-indentation characterization of Ni–Cu–Sn IMC layer subject to isothermal aging. Thin Solid Films **504**, 362–366 (2006). https://doi.org/10.1016/j.tsf.2005.09.056

28. L.C. Tsao, C.H. Huang, C.H. Chung, R.S. Chen, Influence of TiO_2 nanoparticles addition on the microstructural and mechanical properties of Sn0.7Cu nano-composite solder. Mater. Sci. Eng. A **545**, 194–200 (2012). https://doi.org/10.1016/j.msea.2012.03.025

29. A.R. Geranmayeh, R. Mahmudi, M. Kangooie, High-temperature shear strength of lead-free Sn–Sb–Ag/Al_2O_3 composite solder. Mater. Sci. Eng. A **528**, 3967–3972 (2011). https://doi.org/10.1016/j.msea.2011.02.034

30. Y.D. Han, Y. Gao, S.T. Zhang, H.Y. Jing, J. Wei, L. Zhao et al., Study of mechanical properties of Ag nanoparticle-modified graphene/Sn–Ag–Cu solders by nanoindentation. Mater. Sci. Eng. A **761**, 138051 (2019). https://doi.org/10.1016/j.msea.2019.138051

31. Y.D. Han, Y. Gao, H.Y. Jing, J. Wei, L. Zhao, L.Y. Xu, A modified constitutive model of Ag nanoparticle-modified graphene/Sn–Ag–Cu/Cu solder joints. Mater. Sci. Eng. A **777**, 139080 (2020). https://doi.org/10.1016/j.msea.2020.139080

Publisher's Note Springer Nature remains neutral with regard to jurisdictional claims in published maps and institutional affiliations.